Broken and inhomogeneous cloud impact on satellite cloud particle effective radius and cloud-phase retrievals

Erwin L. A. Wolters,[1] Hartwig M. Deneke,[1,2,3] Bart J. J. M. van den Hurk,[1,4]
Jan Fokke Meirink,[1] and Robert A. Roebeling[5]

[1] The impact of sensor resolution on satellite-derived cloud particle effective radius (r_e) and cloud phase (CPH) for broken and overcast inhomogeneous clouds is investigated for the Cloud Physical Properties (CPP) retrieval algorithm used by the Climate Monitoring Satellite Application Facility. First, synthetic data sets of high-resolution (1×1 km^2) and low-resolution (3×3 km^2) radiances are used to illustrate the effect on the r_e and cloud top temperature (CTT) retrieval, the cloud properties that are used for the CPH retrieval. It is shown that low-resolution r_e can be overestimated by up to 12 μm and CTT by up to 20 K for thick broken and inhomogeneous overcast water clouds over ocean and land surfaces. The overestimation of r_e may cause erroneous assignments of "ice" to water clouds. Second, 2 months of CPP retrievals on Moderate Resolution Imaging Spectroradiometer (MODIS) radiances are used to quantify the effect on r_e and CPH over the Atlantic Ocean and central Europe. Over both areas, the low-resolution r_e is overestimated by up to +5 μm for broken and up to 2 μm for inhomogeneous overcast clouds. At low resolution, the fraction of water clouds is underestimated by 2.3% over the Atlantic Ocean and 0.6% over central Europe. The increase of CTT partly compensates for the increase in r_e in the CPH retrievals at low resolution. If no CTT information were used, the underestimation of the water cloud fraction would be 3.5% and 2.2% for the Atlantic Ocean and central Europe, respectively. For inhomogeneous overcast clouds integrated over all inhomogeneity classes, the difference is −1.3% and −2.3% for central Europe and the Atlantic Ocean, respectively. Our results indicate that (1) the retrieval of r_e in the CPP algorithm is sensitive to satellite sensor resolution in case of broken clouds and inhomogeneous overcast clouds and (2) despite this large r_e sensitivity the CPH retrieval is much less sensitive to sensor resolution.

1. Introduction

[2] Clouds strongly affect the Earth's surface energy budget by reflection and absorption of solar and thermal radiation. The way this budget is modulated depends among other things on the particle size distribution, height, and thermodynamic phase of clouds. Water and ice clouds have different radiative properties. For water clouds, the dominant effect is reflection of incoming shortwave radiation and hence a cooling of the atmosphere, whereas for ice clouds absorption

and emission of outgoing terrestrial radiation is dominant, which causes a net warming [*Arking*, 1991; *Hansen et al.*, 1997]. In spite of clouds' great importance, cloud representation in climate models is fairly simplified, owing to both lack of knowledge of the spatiotemporal variation of the various cloud properties and computational constraints.

[3] One of the basic properties necessary for the development of accurate cloud parameterizations is the global distribution of cloud thermodynamic phase, i.e., whether a cloud is composed of either ice or water particles or a combination of both. As noted by *Naud et al.* [2006] in a large-scale assessment of cloud phase and its relationship to atmospheric circulation on climatological time scales, the meteorological conditions under which supercooled liquid water droplets change to ice particles vary widely. A better understanding of cloud phase in both stratiform and cumuliform clouds is necessary for understanding the cloud phase–temperature relationship in the context of diagnosed microphysical processes [*Del Genio et al.*, 1996]. *Roebeling and van Meijgaard* [2009] evaluated the parameterization of cloud amount, cloud

[1]Climate Research and Seismology Department, Royal Netherlands Meteorological Institute, De Bilt, Netherlands.
[2]Meteorological Institute, University of Bonn, Bonn, Germany.
[3]University of Leipzig, Leipzig, Germany.
[4]Institute for Marine and Atmospheric Research Utrecht, Utrecht University, Utrecht, Netherlands.
[5]Research and Development Division, Weather Services, Royal Netherlands Meteorological Institute, De Bilt, Netherlands.

water path (CWP), and cloud phase (CPH) in the Regional Atmospheric Climate Model, RACMO2 [*Lenderink et al.*, 2003] with corresponding data sets obtained from the Spinning Enhanced Visible and Infrared Radiometer Instrument (SEVIRI) on board the Meteosat-8 and Meteosat-9 satellites. It was found that, in general, RACMO2 overestimates the amount of ice clouds by ≈20%. *Weidle and Wernli* [2008] compared spatial and temporal cloud-phase patterns of the European Centre for Medium-Range Weather Forecasts (ECMWF) 40-yr Reanalysis (ERA-40) data over Europe against cloud-phase observations from the POLarization and Directionality of the Earth's Reflectances 1 (POLDER-1) satellite instrument. It was concluded that agreement between the two data sets is good for water and ice clouds; however, the ERA-40 data set contains too many ice clouds for clouds labeled "mixed phase" by POLDER-1.

[4] During the last decades, several cloud-phase retrieval methods from passive imagery data have been proposed using multispectral measurements at solar and infrared wavelengths. Some methods are based on the principle that at near-infrared wavelengths, ice particles absorb solar radiation more effectively than water droplets [*Pilewskie and Twomey*, 1987; *Key and Intrieri*, 2000; *Knap et al.*, 2002; *Platnick et al.*, 2003], while other approaches employ thermal infrared-only wavelengths [*Strabala et al.*, 1994; *Baum et al.*, 2000, 2003; *Turner et al.*, 2003]. The global distribution of cloud thermodynamic phase can among other things be obtained using data from the Moderate Resolution Imaging Spectroradiometer (MODIS) on board the National Aeronautics and Space Administration (NASA) Earth Observing System (EOS) Terra and Aqua satellites.

[5] To discriminate water from ice clouds within the Climate Monitoring Satellite Application Facility (CM-SAF) [*Schulz et al.*, 2009] of the European Organization for the Exploration of Meteorological Satellites (EUMETSAT), a technique was developed using data from visible (0.6 μm), near-infrared (1.6 μm), and thermal infrared (10.8 μm) spectral channels [*Roebeling et al.*, 2006]. The CM-SAF cloud phase determination method has been compared to a 1 year data set of cloud phase obtained from ground-based cloud radar and lidar observations at the Cabauw CloudNET station, Netherlands (see *Illingworth et al.* [2007] for more information on CloudNET). Resulting accuracy (bias) and precision (standard deviation) of the method were established to be <10% and <5%, respectively [*Wolters et al.*, 2008] (also J. Schulz et al., Annual validation report 2008, 2009, available at http://www.cmsaf.eu).

[6] Passive satellite cloud property retrieval techniques rely on the assumption that the observed radiance originates from plane-parallel clouds covering the entire pixel. As a result, when clouds only partly cover a pixel, the observed radiances are an average of the cloudy and cloud-free parts. The contribution of the cloudy part to the total observed radiance depends among others on the fractional cloud coverage, cloud thickness, and albedo of the underlying surface. For broken clouds overlaying a dark surface, the observed radiance at visible and near-infrared wavelengths is reduced due to the clear-sky contribution. As a result, the obtained cloud optical thickness (from the visible) is underestimated and cloud particle effective radius (r_e, from the near infrared) is overestimated [see, e.g., *Barker and Liu*, 1995; *Oreopoulos and Davies*, 1998; *Coakley et al.*, 2005]. In recent years, mainly the 3D effects of cloud property retrievals have been investigated (see, e.g., *Marshak et al.* [2006] and *Iwabuchi and Hayasaka* [2002] for an evaluation of 3D radiative effects on r_e and τ retrievals, respectively). However, the effects of 3D radiative transfer are currently not accounted for in operational cloud property retrievals, both due to computational constraints and due to the fundamental underdeterminedness of the inversion process [*Stephens and Kummerow*, 2007].

[7] At present, a considerable amount of cloud physical property climatologies are derived from geostationary satellite instruments, such as SEVIRI and the Geostationary Operational Environmental Satellite (GOES), as well as polar-orbiting satellite imagers such as Advanced Very High Resolution Radiometer (AVHRR) and MODIS. These platforms differ in sensor resolution, with values of 3×3 to 5×5 km^2 and 1×1 km^2 for the former and latter, respectively. Since about 20% of the clouds are broken clouds as observed from satellite at geostationary satellite resolution [*Deneke et al.*, 2009], and since these clouds have small-scale variability resulting from, e.g., convective updrafts, it can be questioned to what extent the obtained r_e and cloud-phase climatologies at geostationary resolution are influenced by broken cloud fields and inhomogeneous clouds compared to climatologies obtained at polar satellite resolution (typical sampling resolution 1×1 km^2 at nadir). The quantification of the difference between low- and high-resolution cloud physical properties retrievals over various surfaces and for various cloud fractions could serve as a baseline for correcting the low-resolution cloud climatologies. In addition, the difference between low- and high-resolution cloud-phase retrievals can have significant impact on the calculation of the cloud radiative forcing [*Oreopoulos et al.*, 2009].

[8] This paper investigates the impact of broken clouds and overcast inhomogeneous clouds on the retrievals of cloud particle effective radius (r_e) and cloud phase from low-resolution satellite radiances. In this study, the impact of sensor resolution on low-resolution (3×3 km^2 at nadir, but typically 4×7 km^2 at ~50°N) satellite-derived cloud particle effective radius (r_e) and cloud phase (CPH) for broken and overcast inhomogeneous clouds is investigated for the Cloud Physical Properties (CPP) retrieval algorithm used by the CM-SAF. The results presented are limited to a description of differences in retrieved cloud physical properties at two resolutions. The physical causes of these differences are outside the scope of this paper and are subject to future research. Other retrieval algorithms exist that may reveal different sensitivities to resolution degradation, but the selected application illustrates the various relevant processes playing a role.

[9] First, the impact of broken cloudiness and cloud inhomogeneity on the cloud particle r_e retrieval is scrutinized using synthetic data sets. Both the cloud-phase and r_e retrieval of the CPP algorithm rely on an estimate of the particle absorption, which is affected by unresolved variability. Second, for May and August 2007, low- and high-resolution retrievals are obtained from MODIS in two climate regions (subtropical ocean and midlatitude land). These retrievals are interpreted in the context of the synthetic data sets, and the effects on r_e and cloud-phase retrievals are quantified.

[10] The outline of the paper is as follows. Section 2 describes the various MODIS data sets, the CPP algorithm, and the experimental setup of the simulations and retrievals from MODIS radiances. In section 3, the synthetically obtained data sets as well as the comparison of MODIS high- and low-resolution retrievals against these synthetic data sets are shown. Finally, a discussion and conclusions are provided in section 4.

2. Data and Methods

2.1. MODIS Data

[11] MODIS is an imager on board the polar orbiting Terra (equatorial overpass at 1030 local time) and Aqua (equatorial overpass at 1330 local time) satellites. It has 36 onboard calibrated spectral channels with central wavelengths at 0.42–14.2 μm; spatial resolutions are 250 m for bands 1 and 2 (0.65 μm and 0.86 μm), 500 m for bands 3–7 (0.47–2.13 μm), and 1 km for bands 8–36 (4.12–14.2 μm). The data used in this study are the 1 km Level-1B reflectance and radiance data (MOD021KM and MYD021KM) from bands 1 (0.65 μm), 6 (1.64 μm), and 31 (11.0 μm).

[12] Over land, surface albedo information was obtained from 16 day MODIS white-sky albedo maps (the bihemispherical reflectance under conditions of isotropic illumination, MCD43B3 Collection 5 data files). Although we realized that for certain broken cloud cases the usage of a white sky albedo might be less appropriate, the white-sky albedo maps were used for both overcast and broken cloud cases. Over ocean, an albedo of 0.05 was assumed for both the 0.65 μm and 1.64 μm channel, independent of solar zenith angle. It was shown from Scanning Imaging Absorption Spectrometer for Atmospheric Cartography (SCIAMACHY) spectra that ocean surfaces have a similar reflectance at both visible and near-infrared spectral channels [see *Roebeling et al.*, 2006, Figure 2].

[13] Collected data were limited to viewing and solar zenith angles (θ and $\theta_\circ$, respectively) within 60°, because the accuracy and precision of retrieved cloud physical properties decrease for very large θ and $\theta_\circ$ [*Loeb and Coakley*, 1998; *Roebeling et al.*, 2008; *Wolters et al.*, 2008].

2.2. CPP Retrieval Algorithm

[14] In this paper the CPP algorithm of the CM-SAF is used to retrieve r_e and cloud thermodynamic phase [*Roebeling et al.*, 2006] from visible, near-infrared and infrared radiances. The algorithm is operationally applied to radiances observed from SEVIRI on board Meteosat-8 and Meteosat-9 and the AVHRR on board the National Oceanic and Atmospheric Administration (NOAA) satellites. Recent developments enable application of the CPP algorithm to the (nearly) corresponding visible, near-infrared and infrared spectral channels of MODIS [*Deneke et al.*, 2009].

2.2.1. Cloud Masking Procedure

[15] In order to clearly focus on the effects of resolution degradation, we applied a simple, but equivalent cloud mask for both the high- and low-resolution retrievals. This cloud mask is based on the comparison between pixel and clear sky surface (MODIS white-sky albedo) reflectance. Pixels were flagged "cloudy" if the observed 0.6 and 1.6 μm reflectance exceeded the clear-sky value by a predefined threshold value,

i.e., $R_{0.6} > (WS_{0.6} +$ threshold) and $R_{1.6} > WS1.6 +$ threshold, with R and WS referring to the observed reflectance and white-sky albedo, respectively.

2.2.2. Retrieval of τ and r_e

[16] The CPP algorithm relies on the principle that reflectances in the nonabsorbing visible spectral channels (0.6 μm or 0.8 μm) are largely determined by cloud optical thickness, whereas reflectances in the absorbing near-infrared spectral channels (e.g., 1.6 μm, 2.2 μm, and 3.8 μm) are also sensitive to the single scattering albedo of cloud particles, which in turn is a function of cloud particle size and the imaginary part of the refractive index of the cloud particles [*Nakajima and King*, 1990; *Platnick et al.*, 2003]. Cloud optical thickness and cloud particle effective radius are retrieved simultaneously through an iterative comparison of the observed 0.6 μm and 1.6 μm reflectances with Lookup Tables (LUTs) of simulated Radiative Transfer Model (RTM) reflectances for given cloud optical thickness, particle effective radius, and surface albedos for water and ice clouds [*Roebeling et al.*, 2006]. To retrieve τ and r_e, the iteration scheme first searches the LUT for ice clouds, and if no convergence is found, the LUT for water clouds is searched. It is noted that some overlap between large water droplets and small ice crystals causes ambiguities in the phase assignment. In this case, the retrieved τ and r_e values for ice clouds are chosen for pixels when the cloud top temperature (CTT) is smaller than 265 K, while the τ and r_e values for water clouds are chosen for the remaining pixels. In the default CPP algorithm, effective radius values for water (ice) clouds with $\tau < 8$ are relaxed to a climatological value of 8 μm (26 μm), since the r_e retrieval can become ambiguous for such clouds when using a two-channel algorithm [*Nakajima and King*, 1990]. In this paper the relaxation of r_e values to climatological values has been switched off to properly study the effect of broken clouds on the low-resolution r_e retrieval, as otherwise for optically thin clouds r_e values close to the relaxation value of 8 μm would be retrieved.

2.2.3. Retrieval of Cloud Phase

[17] The retrieval of cloud phase is embedded in the τ and r_e iteration scheme of the CPP algorithm. The logical flow of the cloud-phase retrieval algorithm is presented in Figure 1. The phases "water" and "ice" are assigned to pixels for which the measured 0.6 μm and 1.6 μm reflectances correspond to the respective simulated LUT reflectances. In other words, if the τ and r_e retrieval converges for ice clouds, phase "ice" is assigned, while phase "water" is assigned to the remaining cloudy pixels. A CTT check is included. The assignment of phase "ice" is only allowed for CTT <265 K. In about 5% of the cases the r_e retrievals do no convergence for either water or ice clouds. In these cases, phase "ice" is assigned to a pixel with a 1.6 μm reflectance lower than the reflectance of an ice cloud with the largest ice crystals and a CTT lower than 265 K, while phase "water" is assigned to the remaining cloudy pixels. Note that the retrieved cloud phase is not representative for the entire vertical extent of a cloud, but mostly for the cloud top.

[18] The CTT is obtained by correcting the measured 10.8 μm (or 11.0 μm in case of MODIS data) brightness temperature for cloud emissivities (ε_c) less than unity, using the ratio of visible to thermal infrared cloud optical thickness and neglecting thermal infrared scattering [*Minnis et al.*,
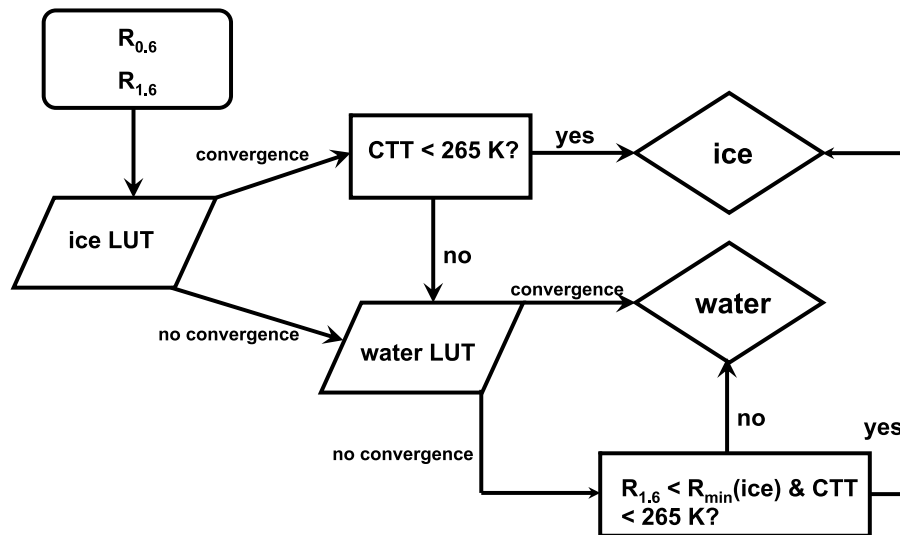
Figure 1. Flowchart of the cloud-phase retrieval algorithm.

1998]. The emissivity correction is not entirely independent of the cloud phase, since the retrieved cloud optical thickness depends on the cloud phase initially retrieved from the LUT search. Because ice crystals have a lower asymmetry factor (less forward scattering of incident radiation) than water droplets, a lower optical thickness is retrieved for ice than water clouds with similar reflectance. To quantify the differences in CTT due to using emissivity corrections for water or ice clouds, we applied the correction twice for about 15000 cloud-flagged pixels. First, all clouds were assumed "water," the second time they were assumed "ice." For clouds having $\tau < 4$ (corresponding to $\varepsilon_c < 0.86$) the average and maximum difference between the two CTT data sets was 0.3 K and 0.7 K, respectively. Thus, it can be concluded that only a marginal dependency of the CTT calculation on the initially retrieved cloud phase exists. Further, in order to avoid too low cloud-top temperatures being retrieved at low emissivity values, a maximum temperature difference of 10 K between the measured brightness temperature and the obtained cloud-top temperature is imposed. Cloud-flagged pixels initially assigned to the phase "ice" are labeled "water" if the cloud-top temperature is warmer than 265 K. Again we note that in the cloud-phase retrieval r_e is not relaxed to the climatological value.

2.2.4. Radiative Transfer Model (RTM) Simulations

[19] The LUT reflectances are simulated with the Doubling Adding KNMI (DAK) [*De Haan et al.*, 1987; *Stammes*, 2001] RTM. This model calculates the monochromatic top-of-atmosphere reflectance in the ultraviolet, visible, and near-infrared, assuming plane-parallel homogeneous clouds over a Lambertian surface. The phase function of water droplets is calculated using Mie theory for spherical particles assuming a Gamma size distribution [*Hansen and Travis*, 1974] with effective radii of 3–24 μm, while ray tracing is used to calculate the phase function for four types of imperfect hexagonal crystals (with volume equivalent effective radii of 6, 12, 26, and 51 μm) of the Cirrus Optical Properties ice crystal library [*Hess et al.*, 1998]. Subsequently, the monochromatic DAK reflectances are converted into spectral band reflectances

using measured SCIAMACHY spectra [*Roebeling et al.*, 2006].

2.3. Synthetic Data Sets

[20] Synthetic cloud data sets at high (1 × 1 km^2 nominal, MODIS-like) and low (3 × 3 km^2 nominal, SEVIRI-like) resolution were constructed to simulate the effects of (1) broken clouds and (2) overcast clouds with an inhomogeneous optical thickness on the retrievals of r_e, CTT and CPH. For clarity, "broken clouds" are defined here as partly cloudy pixels with a constant τ and r_e, while the term "inhomogeneous" is used for overcast clouds with varying τ. The CPP algorithm is used for the cloud property retrievals. Since this algorithm is based on the independent pixel approximation (IPA), three-dimensional cloud radiative effects, such as horizontal photon transport, are not taken into account. The validity of IPA-based methods for these types of studies is discussed in more detail by, for example, *Cahalan et al.* [1994] and *Chambers et al.* [1997a, 1997b]. Hereafter, we refer to SEVIRI-like as low resolution and MODIS-like as high resolution. Further, we define the high-resolution cloud property retrievals averaged to low resolution as HRES and low-resolution retrievals based on radiances averaged to low resolution as LRES.

[21] Figure 2 schematically presents the simulation and retrieval scheme for HRES and LRES, respectively. Solid lines denote the scheme for the retrievals from MODIS data, whereas the dashed lines indicate the flow for the synthetic simulations. For the broken and inhomogeneous cloud field simulations, the LUTs of the CPP algorithm were used to calculate the 0.6 and 1.6 μm reflectances (denoted $R_{0.6,i}$ and $R_{1.6,i}$, respectively, in Figure 2) for predefined high-resolution cloud optical thickness (τ_i) and effective radius ($r_{e,i}$) values. The τ_{HRES} and $r_{e,HRES}$ were computed by averaging τ_i and $r_{e,i}$ over a low-resolution (SEVIRI-like) pixel (see the lower middle box in Figure 2). The τ_{LRES} and $r_{e,LRES}$ were retrieved from simulated SEVIRI-like reflectances (right arrow in Figure 2), which were calculated by averaging
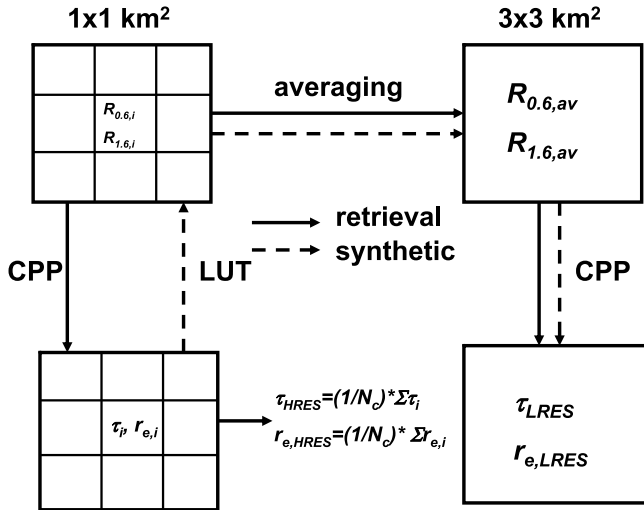
Figure 2. Schematic presentation of the (left) HRES and (right) LRES CPP simulation (indicated by the dashed lines) and retrieval (indicated by the solid lines) schemes. The CPP retrieval algorithm derives τ, r_e, and CPH. The captions "1 × 1 km" and "3 × 3 km" refer to the MODIS and SEVIRI nadir spatial resolutions, respectively. N_c denotes the number of cloudy pixels.

the 1 × 1 km MODIS reflectances to SEVIRI-like resolution (uppermost arrows in Figure 2).

2.3.1. Broken Cloud Simulations

[22] Cloudy pixels were assigned $\tau_i = 8$, $r_{e,i} = 12$ μm to represent thin clouds and $\tau_i = 20$, $r_{e,i} = 12$ μm for thick clouds. These values were chosen based on observed frequency distributions of τ_{HRES} and $r_{e,HRES}$, shown later in Figure 5. Cloud-free pixels were assigned $\tau_i = 0$. Since we assumed that broken clouds are homogeneous, $\tau_{HRES} = \tau_i$ and $r_{e,HRES} = r_{e,i}$. Two surface types were considered, an ocean surface with surface albedo $\alpha_{0.6} = \alpha_{1.6} = 0.05$ and a midlatitude land surface with $\alpha_{0.6} = 0.10$ and $\alpha_{1.6} = 0.20$, with the latter values based on visual inspection of the MODIS white sky albedo data. Once the low-resolution 0.6 and 1.6 μm reflectances were obtained, the CPP algorithm was used to retrieve τ_{LRES} and $r_{e,LRES}$. The simulations were performed for $\theta = \theta_\circ = 10°$ and azimuth difference angle $\phi - \phi_\circ = 100°$. To assess the sensitivity of the simulations to surface albedo heterogeneity, the τ and r_e simulations were repeated for a ±0.03 change in surface albedo at 0.6 μm and 1.6 μm, respectively. The CTT_{LRES} was simulated assuming a CTT_i of 270 K and surface temperatures of 280 K over ocean and 300 K over land surface. Cloudy and cloud-free brightness temperatures were averaged to simulate the brightness temperature at low resolution. Subsequently, τ_{LRES} was used to calculate the cloud emissivity ε_c, after which the CTT_{LRES} was computed.

### 2.3.2. Inhomogeneous Overcast Cloud Simulations

[23] The synthetic inhomogeneous cloud fields were prepared for completely overcast pixels. As for the synthetic broken cloud field data, the simulations were performed for an ensemble of thin and thick water cloud pixels. For thin clouds, τ_i was lognormally distributed around a median value $\tau_{med} = 8$ and $r_{e,i}$ was fixed at 12 μm, while for thick clouds $\tau_{med} = 15$ and $r_{e,i} = 16$ μm. The degree of inhomogeneity within a low-resolution pixel was varied by changing the

spread around τ_{med}, using the normalized interquartile range of τ_i, hereafter referred to as NIQR_τ,

$$\mathrm{NIQR}_\tau = \frac{\tau_{75} - \tau_{25}}{\tau_{50}}, \qquad (1)$$

with τ_{25}, τ_{50}, and τ_{75} denoting the 25th, 50th and 75th percentile value of the τ distribution, respectively. In case of homogeneous overcast clouds ($\mathrm{NIQR}_\tau = 0$), all τ_i and $r_{e,i}$ values were equal. For $\mathrm{NIQR}_\tau > 0$, τ_i values were randomly drawn around the median values $\tau_{med} = 8$ and $\tau_{med} = 15$. The τ_i values to be drawn were constrained to match the desired NIQR_τ within a low-resolution pixel, spanning the range between 0.25 and 1.25. Because the τ_i values were randomly chosen, a large (500) number of pixels were generated. We chose to vary only τ_i (and not also $r_{e,i}$) because, as will be shown later in section 3.1, the observed variability in τ largely exceeds the observed variability in r_e.

[24] To explain the impact of linearly averaging 0.6 and 1.6 μm reflectances on the LRES r_e retrieval, Figure 3 shows the well-known Nakajima-King [*Nakajima and King*, 1990] type plot for these spectral channel reflectances. The solid line denotes an arbitrary r_e curve and the dotted line indicates a curve for larger r_e. The diamond symbols represent two arbitrary 0.6 and 1.6 μm reflectance values for fixed r_e and varying τ. The linear averaging of the pixel reflectance values is indicated by the dashed line. Obviously, linear averaging of the 0.6 and 1.6 μm reflectances causes an overestimation of the cloud absorption at the low resolution, and thus causes an overestimation of r_e. The deviation between low- and high-resolution-retrieved r_e is among others dependent on the curvature of the r_e curve.
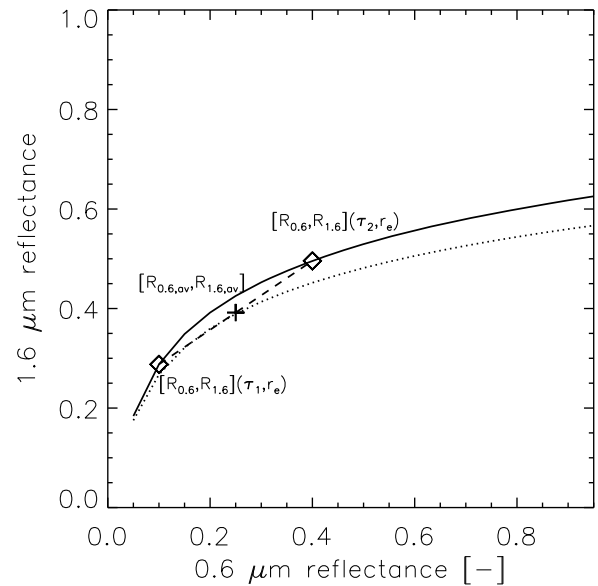
Figure 3. Conceptual plot of the effect of averaging reflectances on the low-resolution r_e retrieval for varying τ and constant r_e. The solid line indicates an arbitrary r_e curve. The diamonds denote the reflectance pairs $[R_{0.6}, R_{1.6}]$ at τ_1 and τ_2. The cross shows the mean $[R_{0.6,av}, R_{1.6,av}]$ value; the deviation from the solid line is obvious and leads to a larger low-resolution-retrieved r_e (indicated by the dotted line).
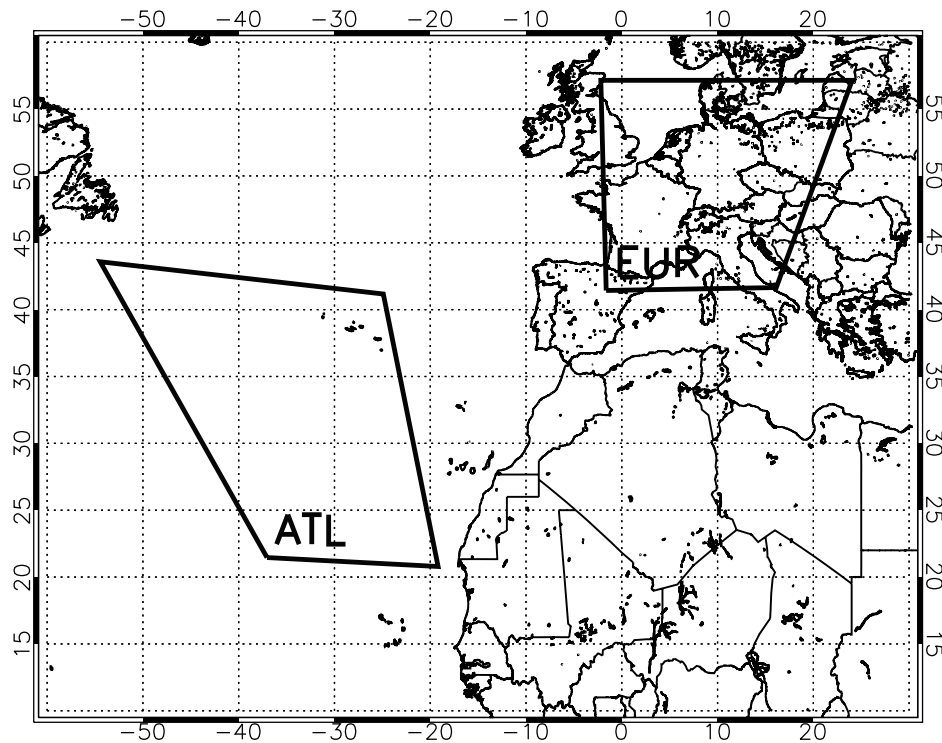
Figure 4. The two areas of investigation: eastern Atlantic Ocean (ATL) and central Europe (EUR).

2.4. Aggregation of MODIS Observations

[25] The cloud physical property data sets were retrieved for the areas shown in Figure 4 for May and August 2007 from MODIS Level-1 and Level-2 data with a version of the CPP algorithm that was adapted for using MODIS reflectances. τ_{HRES}, τ_{LRES}, $r_{e,HRES}$, $r_{e,LRES}$, CPH_{HRES}, and CPH_{LRES} were obtained following the procedure described in Figure 2. As indicated in section 2.1, we applied a rather simple cloud masking technique based on the observed clear-sky reflectances at 0.6 μm and 1.6 μm. The HRES CPP retrievals were computed by averaging the 1×1 km τ_i and $r_{e,i}$ over a SEVIRI pixel.

[26] LRES retrievals were obtained from MODIS 1×1 km radiances and surface albedos, which were averaged to the SEVIRI resolution. It is noted that the 1×1 km MODIS radiances were averaged to the real SEVIRI resolution, rather than to a fixed 3×3 or 5×5 pixel grid. By doing so, a SEVIRI image of the investigated area was reproduced. The number of 1×1 km pixels to be aggregated within a SEVIRI pixel was 5–35, dependent on the MODIS viewing angle and the SEVIRI pixel size at the geolocation of observation. Using the MODIS land/sea mask, only pixels over ocean and land were selected for the ATL and EUR area, respectively. Additional statistics on cloud fraction, the fraction of water and ice clouds, and variability in cloud optical thickness were also calculated for SEVIRI pixels having at least 10 MODIS pixels.

3. Results

3.1. Description of Observed Cloud-Type Occurrence Over ATL and EUR

[27] Table 1 shows the HRES and LRES distribution of water, ice, and mixed phase clouds for the classes cloud-free,

broken cloud, and overcast. The mixed-phase categorization represents HRES pixels with varying phases within the domain. All percentages are relative to the total number of observations for the ATL and EUR area, being 269,000 and 154,000, respectively. About 20% of the clouds are broken clouds, which is consistent with the findings of *Deneke et al.* [2009]. It follows from Table 1 that over the EUR area clouds contain considerably more ice than over the ATL area, especially for the fully overcast cases. This probably relates to deep convection, which dominates cloud formation over the European continent during the summer season. Over the ATL area, cloud vertical extent is limited due to both less convection and subsidence within a quasi-persistent high-pressure area.

[28] Figure 5 shows contour plots of retrieved τ and r_e for broken clouds over the EUR and ATL areas. Only pixels labeled as "water" at HRES are included. Figure 5 shows that

Table 1. Water and Ice Cloud Occurrence Frequencies Based on HRES and LRES Retrievals for May and August 2007[a]

Class	Cloud Phase	ATL (%)		EUR (%)	
		HRES	LRES	HRES	LRES
Cloud-free		42.3	42.4	28.1	28.0
Broken clouds	water	6.0	8.3	2.1	7.3
	ice	0.6	1.5	5.6	11.1
	mixed	3.2	–	10.7	–
Overcast	water	29.1	29.5	14.0	16.6
	ice	15.2	18.3	33.0	37.0
	mixed	3.6	–	6.4	–

[a]Only clouds with $\tau_{HRES} > 1.0$ were included in the data set.
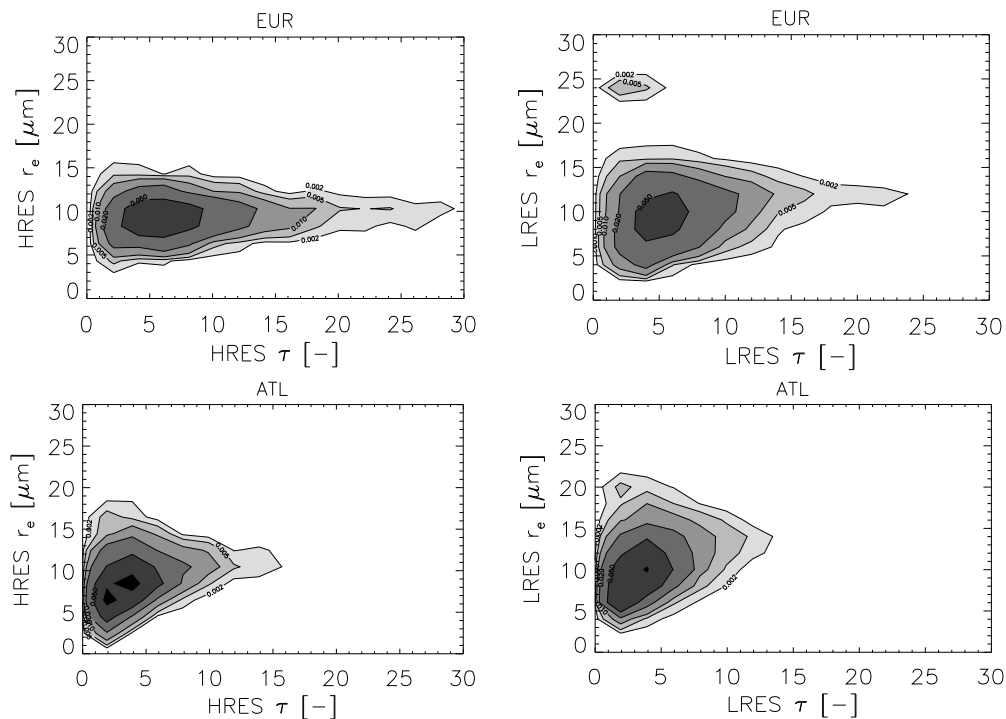
Figure 5. Contour plots of (left) HRES-retrieved and (right) LRES-retrieved τ versus r_e for broken water clouds over the (top) EUR and (bottom) ATL areas for May and August 2007. Contour intervals are plotted at occurrence frequencies of 0.002, 0.005, 0.01, 0.02, and 0.05.

for both the ATL and EUR area at LRES, τ is lower than at HRES and that r_e increases from HRES to LRES. The increase of r_e with increasing τ confirms findings of *Szczodrak et al.* [2001].

[29] Since the low-resolution r_e retrieval could be influenced by variability in both the high-resolution τ and r_e, we have performed calculations on the variability in τ and r_e within the LRES pixels over both the ATL and EUR area. The two quantities are shown in Figure 6. For consistency reasons, both the τ and r_e variability have been calculated using the NIQR as defined by equation (1). From Figure 6 it is obvious that the variability in τ largely exceeds the variability of r_e. The median NIQR values are 0.451 and 0.147 for τ and r_e, respectively.

3.2. Simulations With Synthetic Data

3.2.1. Broken Clouds

[30] Figure 7 shows the simulated τ_{LRES}, $r_{e,LRES}$, and CTT_{LRES} for water clouds over an underlying dark and bright surface. The error bars in Figures 7c and 7d denote the variability in retrieved r_e resulting from a ±0.03 change in 1.6 μm surface albedo. The τ_{LRES} increases nearly linearly with cloud fraction for both the thin and thick clouds (Figures 7a and 7b), independent of the underlying surface.

[31] For thin clouds (Figure 7c), $r_{e,LRES}$ is larger than $r_{e,HRES}$ for all cloud fractions. Further, $r_{e,LRES}$ is larger over a (dark) ocean than over a (brighter) land surface. Because effective radius increases with decreasing 1.6 μm reflectance, the resulting increase in $r_{e,LRES}$ is larger over a dark surface than over a bright surface.

[32] Figure 7d shows that also for thick clouds ($\tau_{HRES} = 20$, $r_{e,HRES} = 12 \mu$m), $r_{e,LRES}$ is larger than $r_{e,HRES}$ with the largest

overestimation again occurring over the ocean surface. In addition to the surface albedo effect, $r_{e,LRES}$ approaches 24 μm, the maximum value for water clouds in the LUT, over the dark surface and for cloud fraction ≤0.4. In this case, the inversion of 0.6 μm and 1.6 μm reflectances in the CPP algorithm results in the retrieval of an ice particle effective radius and in principle the assignment of cloud phase "ice." The cloud-top temperature as function of cloud fraction is shown in Figures 7e and 7f. It can be seen that CTT_{LRES}
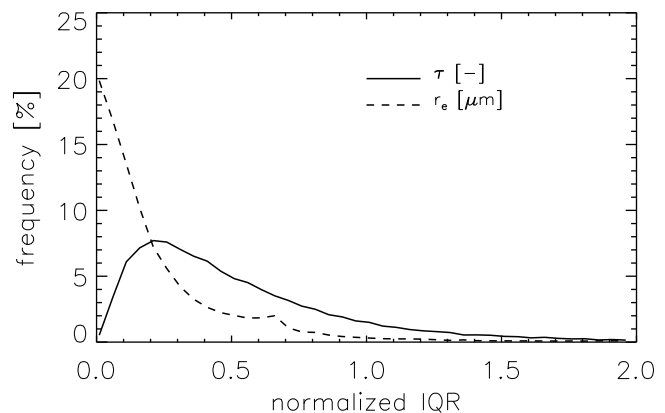
Figure 6. Frequency distribution of the variability in τ (solid line) and r_e (dashed line), both expressed as normalized interquartile range (see equation (1) for its definition). Data were selected over both areas for May and August 2007; within each LRES pixel the interquartile range and median r_e and τ of the HRES retrievals were computed.
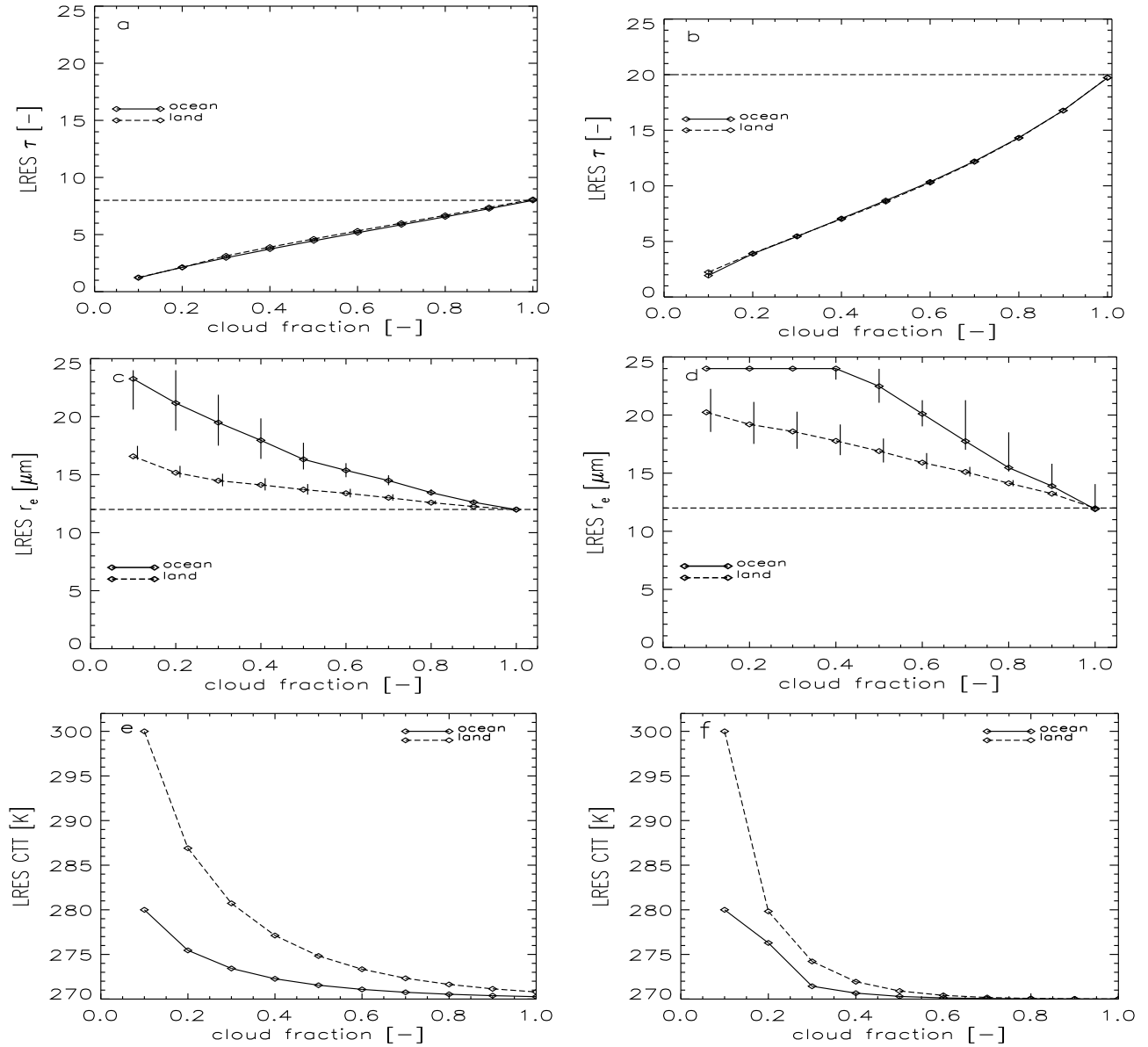
Figure 7. Simulation results for broken clouds: (a, b) Simulated τ_{LRES}, (c, d) $r_{e,LRES}$, and (e, f) and low-resolution CTT as function of cloud fraction for a thin water cloud with $\tau = 8$, $r_e = 12$ μm (Figures 7a, 7c, and 7e) and a thick water cloud with $\tau = 20$, $r_e = 12$ μm (Figures 7b, 7d, and 7f). Calculations were performed for a dark (ocean, $\alpha_{0.6} = \alpha_{1.6} = 0.05$, solid line) and bright (midlatitude land, $\alpha_{0.6} = 0.10$, $\alpha_{1.6} = 0.20$, dashed line) surface. Vertical bars denote the spread in retrieved τ and r_e when assuming an error in the 0.6 μm (for τ) or 1.6 μm (for r_e) surface albedo of ±0.03. The horizontal dashed lines indicate τ_{HRES} (Figures 7a and 7b) and $r_{e,HRES}$ (Figures 7c and 7d). Solar ($\theta\circ$) and viewing (θ) zenith angles are 10°, and the azimuth difference angle ($\phi - \phi\circ$) is 100°. CTT was calculated assuming a real cloud top temperature of 270 K and surface temperatures of 280 K and 300 K for the ocean and midlatitude land surface, respectively.

quickly converges to the real cloud-top temperature (270 K) as a result of the cloud emissivity correction. From Figure 7f it also follows that $\varepsilon_{c,LRES}$ approaches unity at lower cloud fractions in case of optically thick clouds at high resolution, hence the real cloud-top temperature is more rapidly converging. It is recalled that due to the underestimation of τ_{LRES}, $\varepsilon_{c,LRES}$ is also underestimated, and hence CTT$_{LRES}$ is overestimated. Since broken cloudiness mostly occurs for cumulus (water) clouds, the overestimation made in CTT due to an underestimation of ε_c provides a partly

compensating factor for the overestimation due to broken clouds in r_e.

3.2.2. Inhomogeneous Overcast Clouds

[33] Figure 8 presents the simulated difference (Δr_e) between $r_{e,HRES}$ and $r_{e,LRES}$ for overcast inhomogeneous clouds with $\tau_{med} = 8$ and $\tau_{med} = 15$. Because $r_{e,HRES}$ was fixed at 12 μm and 16 μm in Figures 8a and 8b, respectively, the variation in $r_{e,LRES}$ is solely caused by a variation in τ_i.

[34] The $r_{e,LRES}$ becomes larger than $r_{e,HRES}$ with increasing inhomogeneity for both cloud types, with the largest
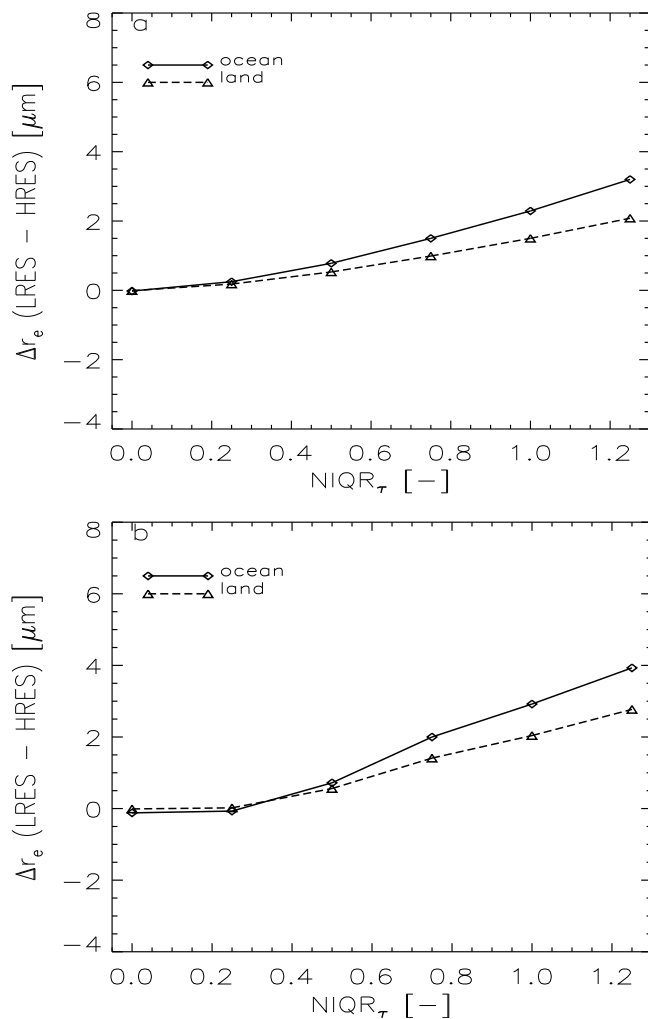
Figure 8. Difference between simulated $r_{e,LRES}$ and $r_{e,HRES}$ (Δr_e) for overcast water clouds as function of cloud inhomogeneity, expressed as normalized interquartile range of τ ($NIQR_\tau$; see text for its definition). Results are shown for a dark (solid line) and bright surface (dashed line) at 1.6 μm for (a) thin clouds with HRES $\tau_{med} = 8$ and $r_e = 12$ μm and (b) thick clouds with $\tau_{med} = 15$ and $r_e = 16$ μm.

differences occurring over a dark surface, due to the larger contrast between cloud and surface compared to a bright surface. For larger $r_{e,HRES}$ (Figure 8b) the effect of inhomogeneous clouds on $r_{e,LRES}$ is larger, which is related to the steeper curvature of the r_e vs τ function for larger cloud particles. As a result, linearly averaging of reflectances leads to a larger deviation from $r_{e,HRES}$ (see Figure 3).

[35] Figure 9 shows Δr_e as function of τ_{med} at $NIQR_\tau = 1.25$ for overcast water clouds over an ocean surface having large ($r_e = 16$ μm) and small ($r_e = 12$ μm) droplets. The effect of the steeper curvature at $r_e = 16$ μm can clearly be seen. At low τ_{med}, the difference between thick and thin water clouds becomes larger. This is because of a larger sensitivity to a change in 1.6 μm reflectance for larger r_e values. For example, at $\tau = 4$ the sensitivity to a 1% change in 1.6 μm reflectance is $\approx$1.5 μm larger within the range 16–24 μm than within the range 12–16 μm. The simulations for inhomoge-

neous overcast clouds show that at larger degrees of inhomogeneity and for clouds with large droplet sizes (generally present in thicker clouds) the $r_{e,LRES}$ is considerably overestimated, which may lead to erroneous CPH_{LRES} retrievals.

3.3. MODIS Observations

[36] The evaluation of simulated CPP retrievals in the previous section demonstrated that for broken clouds the largest effect on the low-resolution r_e and CPH retrieval occurs for thick clouds, whereas for inhomogeneous overcast clouds the low-resolution r_e and CPH retrievals are most affected for thin clouds having large particles. Both the broken and inhomogeneous cloud effects are most prominent over dark surfaces, although the CTT check may have a compensating contribution. To quantify the effects of broken and inhomogeneous clouds in true observations, the CPP algorithm is used to compare HRES and LRES retrievals from MODIS radiances. First, the effect of broken and inhomogeneous clouds on the retrieval of r_e is quantified for the ocean (ATL) and midlatitude land (EUR) area. Second, the effect on the retrieval of cloud phase is assessed.

3.3.1. Broken Clouds

[37] It follows from Table 1 that about 20% of the clouds are broken. In order to exemplify where differences between HRES- and LRES-retrieved r_e occur, Figure 10 shows the HRES- and LRES-obtained r_e for an area southeast of the Azorean archipelago. This area is frequently covered with stratocumulus fields within a semipersistent high-pressure area. It is obvious from Figure 10 that the largest overestimations at LRES occur at the (optically thin) stratocumulus edges.

[38] Figure 11 presents the mean $r_{e,HRES}$ and $r_{e,LRES}$ versus cloud fraction for the EUR and ATL area for water clouds. Cloud-free pixels and pixels with $\tau_{HRES} < 1$ were
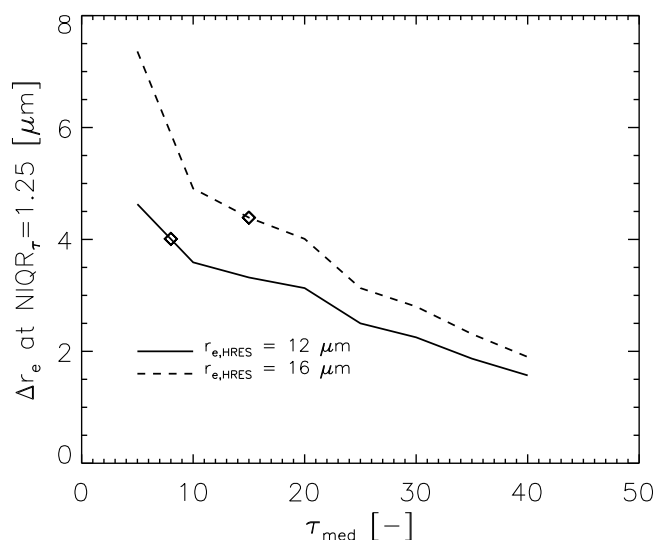
Figure 9. Simulated Δr_e at $NIQR_\tau = 1.25$ over a dark surface ($\alpha_{0.6} = \alpha_{1.6} = 0.05$) as a function of τ_{med} for overcast water clouds having small ($r_e = 12$ μm, solid line) and large ($r_e = 16$ μm, dashed line) droplets. The values at $NIQR_\tau = 1.25$ over a dark surface shown in Figures 8a and 8b are denoted by the diamond symbols.
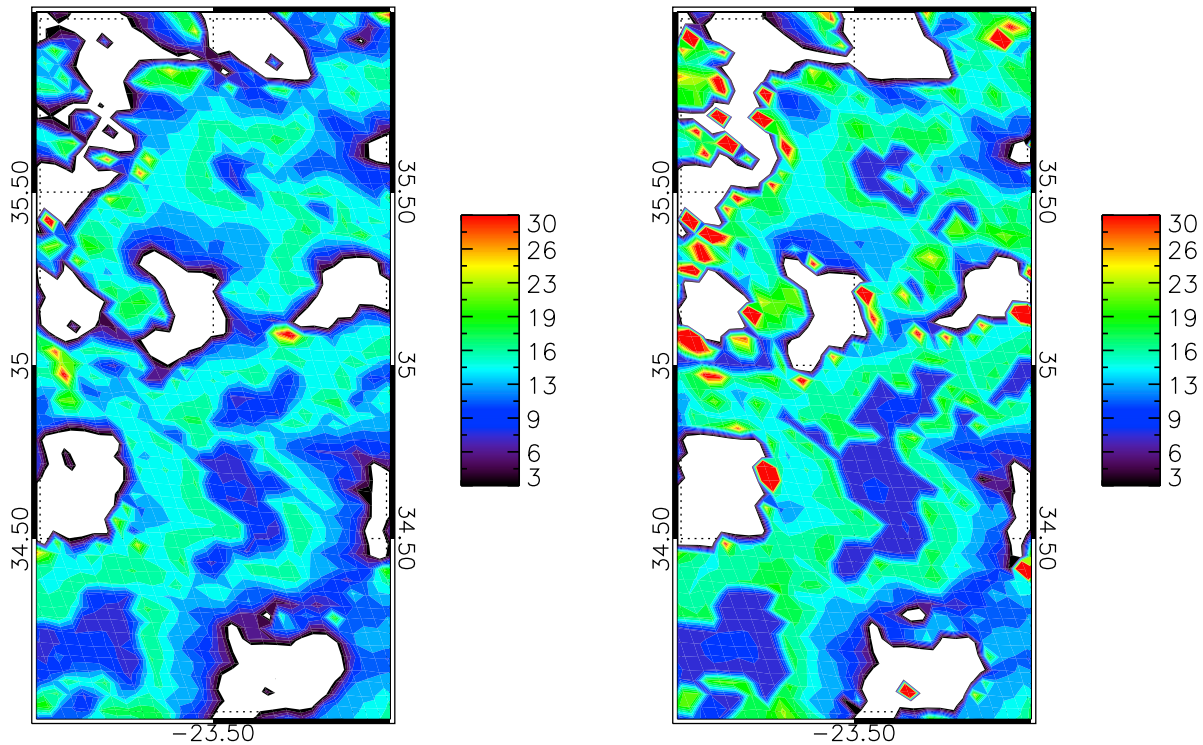
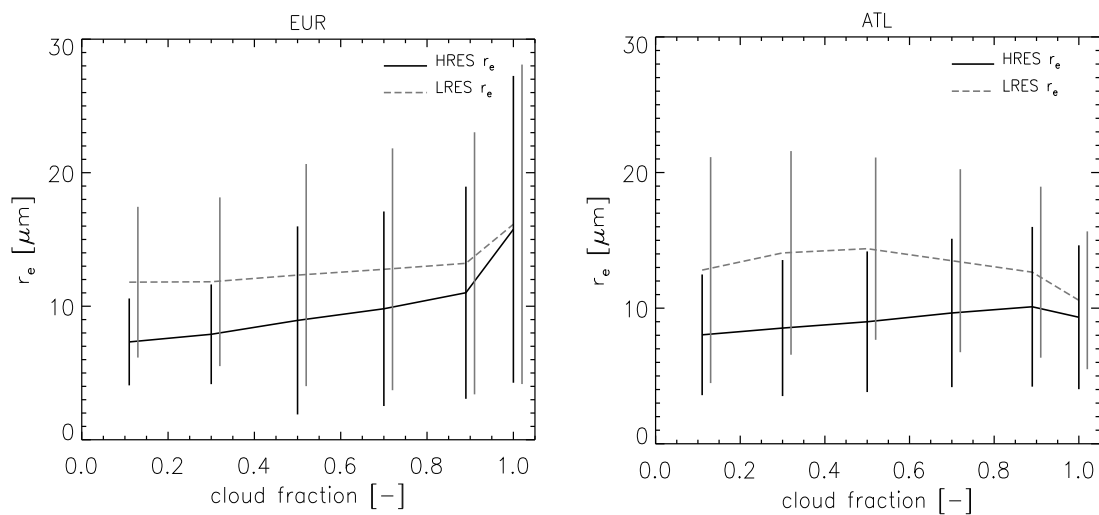**Figure 10.** (left) HRES-retrieved and (right) LRES-retrieved r_e (μm) over a $1° \times 2°$ area southeast of the Azores. Clouds with $r_e < 3$ are not shown. Contouring is done for each 3 μm interval.

discarded to ensure that only clouds were investigated, rather than also thick aerosol layers. Over the EUR area, the largest difference between $r_{e,LRES}$ and $r_{e,HRES}$ occur at the lowest cloud fractions (+4 μm at cloud fractions 0.02–0.2), which is conform the simulations shown in Figure 7. However, differences are smaller than in the synthetic data. The use of a fixed r_e and viewing geometry in the simulations is probably

responsible for this. The difference $r_{e,LRES} - r_{e,HRES}$ gradually decreases toward +0.5 μm at cloud fraction 1.0.

[39] Similar to the EUR area, over the ATL area the largest differences $r_{e,LRES} - r_{e,HRES}$ are found at low cloud fractions. The difference between $r_{e,LRES}$ and $r_{e,HRES}$ for broken clouds is on the same order (5 μm at the lowest cloud fraction bin) as found by *Coakley et al.* [2005], despite that less sensitive

Figure 11. Mean retrieved $r_{e,HRES}$ (black line) and $r_{e,LRES}$ (dashed grey line) for water clouds (at both HRES and LRES) retrieved from MODIS radiances as function of cloud fraction for the (left) EUR and (right) ATL areas. The vertical bars indicate the standard deviations within the respective cloud fraction bins (centered at 0.1, 0.3, 0.5, 0.7, and 0.9, and for cloud fraction = 1.0). For clarity of presentation, the vertical bars of $r_{e,LRES}$ are slightly shifted to the right. Only clouds with $\tau_{HRES} > 1$ were included.
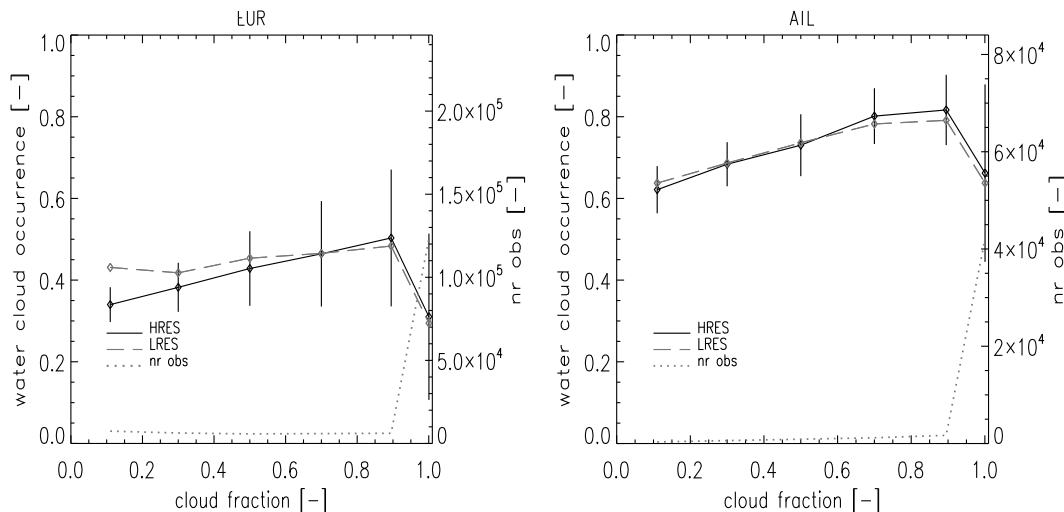
Figure 12. HRES-retrieved (solid line) and LRES-retrieved (dashed grey line) CPH expressed as water cloud occurrence frequency versus cloud fraction for clouds with $\tau_{HRES} > 1$ over the (left) EUR and (right) ATL areas. Vertical bars denote the standard deviations of the HRES obtained water cloud occurrence frequency. The number of observations for each cloud fraction bin is indicated by the dotted grey line, with scaling on the right-hand axis. The CPH was retrieved using both the 0.6 and 1.6 μm reflectances and the CTT correction (see section 2.2 for more details).

spectral channels were used for retrieving r_e by *Coakley et al.* [2005] as a result of more absorption and hence a smaller penetration depth inside a cloud [*Rosenfeld et al.*, 2004].

[40] The HRES- and LRES-retrieved water cloud occurrence frequency (hereafter referenced as CPH$_{HRES}$ and CPH$_{LRES}$, respectively) versus cloud fraction is shown in Figure 12 for the EUR and ATL areas for clouds with $\tau_{HRES} > 1$. Over the EUR area, CPH$_{LRES}$ − CPH$_{HRES}$ is ≈+10% at low cloud fractions, but decreases and changes sign at −2% at cloud fraction >0.9. Integrated over all cloud fractions the difference CPH$_{LRES}$ − CPH$_{HRES}$ is −0.6%. Without CTT check the difference CPH$_{LRES}$ − CPH$_{HRES}$ would be −2.2%, which indicates the added value of this check to the cloud-phase retrieval.

[41] Over the ATL area, the difference CPH$_{LRES}$ − CPH$_{HRES}$ is small over all cloud fractions, ranging from +1% at cloud fraction 0.1 toward −3% for fully overcast clouds. Integrated over all cloud fractions, the difference CPH$_{LRES}$ − CPH$_{HRES}$ is −2.3%. If no CTT check would be included in the cloud-phase retrieval algorithm, the integrated difference would be −3.5%.

3.3.2. Inhomogeneous Overcast Clouds

[42] For the entire data set of both areas, within each SEVIRI pixel the 25th, 50th, and 75th percentiles of τ_i were calculated, from which the NIQR$_\tau$ within the respective LRES pixel was obtained. Subsequently, SEVIRI pixels were collected within NIQR$_\tau$ bins of 0.0–0.05 (representing virtually homogeneous clouds), 0.05–0.5, 0.5–1.0, and 1.0–1.5. For each bin the mean and standard deviation of Δr_e was computed.

[43] Figure 13 presents the observed mean difference between $r_{e,LRES}$ and $r_{e,HRES}$ (Δr_e) for HRES-retrieved water clouds with $\tau_{HRES} > 1$. For reference, also the differences found in the synthetic data set with fixed values of $r_e = 12$ μm and $\tau_{med} = 8$ (Figure 8a) are shown. Figure 13 demonstrates that for both the EUR and ATL area the observed Δr_e follows

a similar trend with increasing cloud inhomogeneity as the Δr_e from the synthetic data, although the retrieved values are substantially lower than the synthetic values. Differences between synthetic and observed Δr_e can be attributed to differences between the τ distributions; in the synthetic data sets a lognormal distribution was used, whereas the τ distributions in the retrievals may deviate from this. Also, the assumed fixed value of $r_{e,i}$ and viewing geometry in the synthetic data sets is in contrast with the MODIS observations.

[44] CPH$_{HRES}$ and CPH$_{LRES}$ are plotted versus cloud inhomogeneity for EUR and ATL in Figure 14. Over the EUR area, CPH$_{LRES}$ and CPH$_{HRES}$ gradually diverge with increasing inhomogeneity reaching a difference of 10% more "ice" than "water" retrieved at LRES than at HRES for NIQR$_\tau$ = 1.25. Integrated over all inhomogeneity bins, the difference CPH$_{LRES}$ − CPH$_{HRES}$ is −1.3%. Over the ATL area, CPH$_{LRES}$ < CPH$_{HRES}$ within the entire range of inhomogeneities, which is most likely linked to the increase in $r_{e,LRES}$ with increasing cloud inhomogeneity, as seen from both the simulations and observations (see Figures 8 and 13). The difference CPH$_{LRES}$ − CPH$_{HRES}$ reaches a value of −6% at NIQR$_\tau$ = 0.75 and NIQR$_\tau$ = 1.25, resulting in an integrated difference of −2.5%.

4. Discussion and Conclusions

[45] In this paper we investigated the influence of broken cloudiness and cloud inhomogeneity on satellite-retrieved r_e and cloud phase of the CPP retrieval algorithm, and quantified the difference between low-resolution (geostationary satellite) and high-resolution (polar satellite) derived values. We have identified an overestimate of cloud particle absorption caused by the nonlinear relation of reflectances at absorbing and nonabsorbing wavelengths as underlying physical mechanism. For the sake of simplicity, the inhomogeneity effect was only investigated for overcast cloud
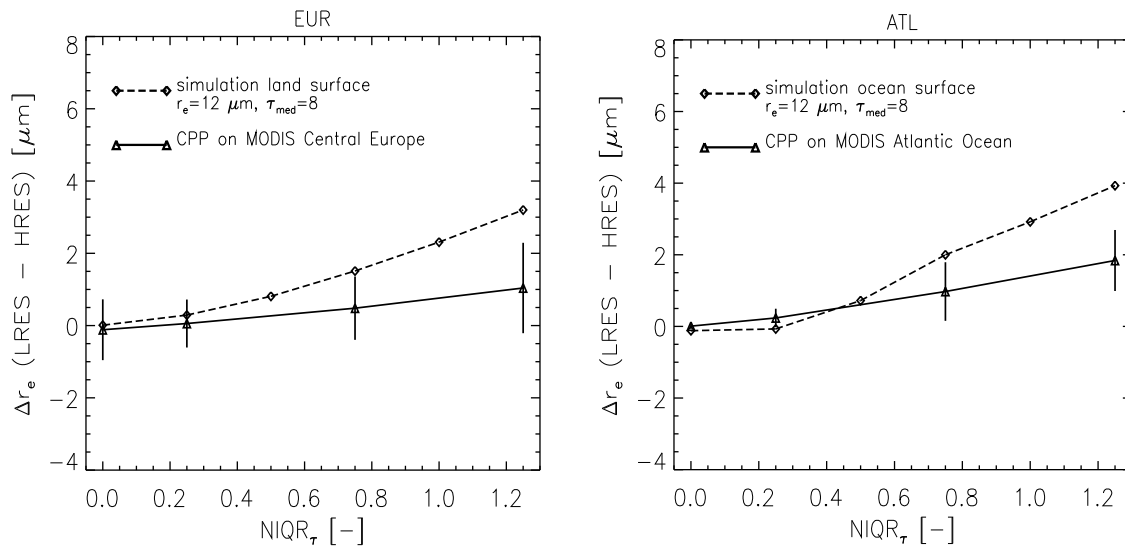
Figure 13. Comparison between MODIS-observed (solid line) and simulated (dashed line) Δr_e for overcast inhomogeneous HRES-retrieved water clouds with $\tau_{HRES} > 1$ as function of $NIQR_\tau$ for (left) EUR and (right) ATL. The triangles denoting the observed values are plotted at the $NIQR_\tau$ bin center, and vertical bars denote the observed standard deviation of Δr_e within each bin.

cases. Using synthetic data sets, it was shown that for thick broken clouds at high resolution (1×1 km^2 nominal) the low-resolution (3×3 km^2 nominal) CPH retrieval can become erroneous due to a too high retrieved r_e (by up to 12 μm). This effect is strongest over dark surfaces (ocean), as the high-resolution cloud-free reflectances significantly contribute to the low-resolution 0.6 and 1.6 μm reflectance. For inhomogeneous overcast clouds, $r_{e,LRES}$ can be overestimated by 3–4 μm for both clouds with $r_{e,HRES} = 12$ μm and clouds with $r_{e,HRES} = 16$ μm, depending on the degree of inhomogeneity and underlying surface. The overestimation of $r_{e,LRES}$ is larger than the findings of *Zinner and Mayer* [2006], who found about 5% overestimation in low-resolution r_e for

inhomogeneous overcast clouds. However, their analysis included both inhomogeneity and 3D effects, while the latter was not accounted for in our 1D simulations.

[46] Retrievals for broken cloud fields from MODIS radiances for May and August 2007 reveal that over both the ATL and EUR area $r_{e,LRES}$ is up to 5 μm larger than $r_{e,HRES}$. The overestimation of $r_{e,LRES}$ is conform the simulations for broken cloud $r_{e,LRES}$, although the magnitude of the observed difference is smaller than the simulated difference, due to the use of a fixed $r_{e,HRES}$ and viewing geometry in the simulations.

[47] For cloud phase, for cloud fractions smaller than 0.5 the difference $CPH_{LRES} - CPH_{HRES}$ is up to +10% over
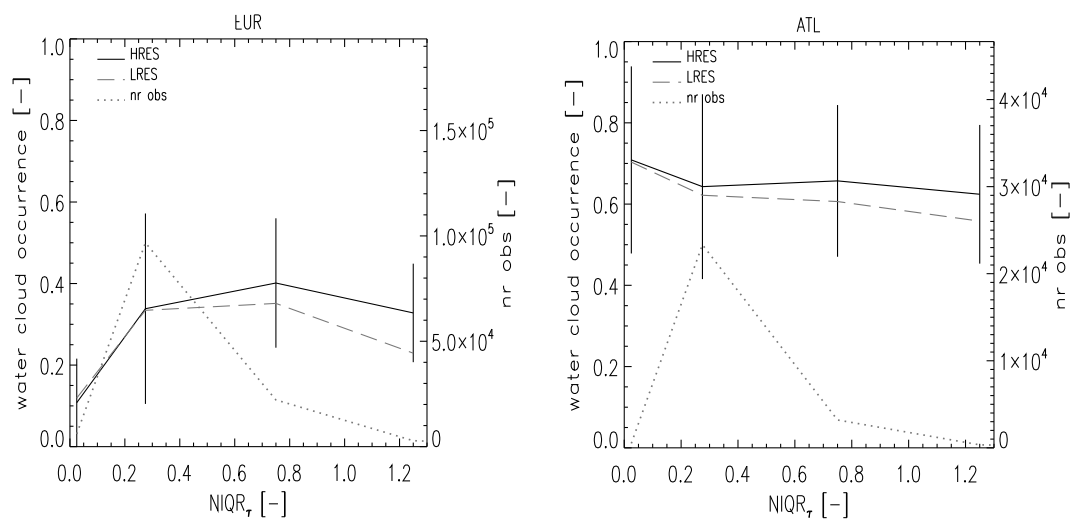
Figure 14. Water cloud occurrence frequency as function of cloud inhomogeneity ($NIQR_\tau$) obtained from HRES (solid line) and LRES (dashed line) retrievals for overcast clouds with $\tau_{HRES} > 1$. The dotted grey line indicates the number of observations per $NIQR_\tau$ bin, with scaling on the right-hand axis. The CPH was retrieved using both the 0.6 and 1.6 μm reflectances and the CTT correction (see section 2.2 for more details).

the EUR area, while this difference becomes −2% at larger cloud fractions. Integrated over all cloud fractions, 0.6% less water clouds are retrieved at LRES than at HRES. If no CTT check is applied, 2.2% less water clouds would be retrieved at LRES. Over the ATL area, $CPH_{LRES} − CPH_{HRES}$ gradually decreases from +1% to −3% with increasing cloud fraction. Due to the number of observations being strongly skewed toward overcast clouds, the overall difference is −2.3%. If no CTT check is applied, this difference would be −3.5%.

[48] For inhomogeneous overcast clouds, the difference $r_{e,LRES} − r_{e,HRES}$ (Δr_e) gradually increases with increasing inhomogeneity, but more pronounced in the synthetic data than from MODIS retrievals. Maximum observed Δr_e values are +1 μm and +2 μm over the EUR and ATL area, respectively. It is argued that the difference between synthetic data and retrievals is caused by differences in the τ distributions, in the variability in $r_{e,i}$ and viewing geometries in the retrievals. The difference $CPH_{LRES} − CPH_{HRES}$ integrated over all inhomogeneity classes is −1.3% and −2.5% over the EUR and ATL area, respectively.

[49] The problem of broken cloudiness is not constrained to using visible/near-infrared data only; other r_e and cloud-phase retrieval methods likely will have different values at low and high resolution. However, the sensitivity to surface albedo or surface emissivity (in case of a thermal infrared retrieval method) will depend on the spectral channels used. For example, use of the 2.2 μm or 3.9 μm channel for retrieving r_e will be less sensitive to the underlying surface than the 1.6 μm channel used here, since cloud particles absorb radiation more efficiently at the former wavelengths and thus decrease the amount of radiation penetrating through a cloud. The stronger absorption of the AVHRR 3.7 μm channel compared to the 1.6 μm channel enabled *Platnick et al.* [2001] to improve r_e retrievals over snow-covered areas in the Arctic region.

[50] The upcoming generation of geostationary satellite imagers will carry one or more high spatial resolution channels in addition to the suite of spectral channels that observe at the operational resolution. These high-resolution channels may allow for correcting the low-resolution r_e and CPH (as well as other cloud physical properties) climatologies by using the fractional coverage and/or horizontal inhomogeneity of cloud fields obtained at high resolution. For the SEVIRI instrument, attempts are ongoing to retrieve high-resolution (1 × 1 km^2 at nadir) τ from the high-resolution visible (HRV) channel, which spans the wavelength range of ~0.4–1.1 μm [*Deneke and Roebeling*, 2010]. Despite this channel having different spectral characteristics than the low-resolution 0.6 μm channel, an estimate of the high-resolution τ is made by using the correlation between HRV reflectance averaged over a low-resolution pixel and the corresponding low-resolution 0.6 μm reflectance. Further, an estimate of cloud fraction using a simple HRV reflectance threshold can be obtained to correct the low-resolution 0.6 and 1.6 μm reflectance for cloud fraction before the low-resolution CPP retrieval is performed. In order to develop a robust correction method, differences between the HRV reflectance and 0.6 μm reflectance need to be investigated over various areas and for various cloud types.

[51] For cloud inhomogeneity, alternatives to the NIQR diagnostic used to obtain cloud variability information exist, for example, the variance in measured visible radiances or the CTT. It is expected that different cloud inhomogeneity indicators likely give slightly different results than presented here. However, the general pattern seen for $r_{e,LRES}$ and CPH_{LRES} with increasing cloud inhomogeneity will dominate. The above results, including our ongoing research on the correlation between high- and low-resolution reflectance, will be an important improvement to the low-resolution derived cloud physical property climatologies. Future work will focus on implementation of bias correction factors to the cloud property climatologies derived at geostationary resolution.

References

Arking, A. (1991), The radiative effects of clouds and their impact on climate, *Bull. Am. Meteorol. Soc.*, *72*, 795–813.

Barker, H. W., and D. Liu (1995), Inferring optical depth of broken clouds from Landsat data, *J. Clim.*, *8*, 2620–2630.

Baum, B. A., P. F. Soulen, K. I. Strabala, M. D. King, S. A. Ackerman, W. P. Menzel, and P. Yang (2000), Remote sensing of cloud properties using MODIS Airborne Simulator imagery during SUCCESS: 2. Cloud thermodynamic phase, *J. Geophys. Res.*, *105*, 11,781–11,792.

Baum, B. A., R. A. Frey, G. G. Mace, M. K. Harkey, and P. Yang (2003), Nighttime multilayered cloud detection using MODIS and ARM data, *J. Appl. Meteorol.*, *42*, 905–919.

Cahalan, R. F., W. Ridgway, W. J. Wiscombe, S. Gollmer, and Harshvardhan (1994), Independent pixel and Monte Carlo estimates of stratocumulus albedo, *J. Atmos. Sci.*, *51*, 3776–3790.

Chambers, L. H., B. A. Wielicki, and K. F. Evans (1997a), Independent pixel and two-dimensional estimates of Landsat-derived cloud field albedo, *J. Atmos. Sci.*, *54*, 1525–1532.

Chambers, L. H., B. A. Wielicki, and K. F. Evans (1997b), Accuracy of the independent pixel approximation for satellite estimates of oceanic boundary layer cloud optical depth, *J. Geophys. Res.*, *102*, 1779–1794.

Coakley, J. A., M. A. Friedman, and W. R. Tahnk (2005), Retrieval of cloud properties for partly cloudy imager pixels, *J. Atmos. Oceanic Technol.*, *22*, 3–17.

De Haan, J. F., P. B. Bosma, and J. W. Hovenier (1987), The adding method for multiple scattering calculations of polarized light, *Astron. Astrophys.*, *183*, 371–391.

Del Genio, A. D., M. S. Yao, W. Kovari, and K. K. W. Lo (1996), A prognostic cloud water parameterization for global climate models, *J. Clim.*, *9*, 270–304.

Deneke, H. M., and R. A. Roebeling (2010), Downscaling of METEOSAT SEVIRI 0.6 and 0.8 micron channel radiances utilizing the high-resolution visible channel, *Atmos. Chem. Phys. Discuss.*, *10*, 10,707–10,740.

Deneke, H. M., R. A. Roebeling, E. L. A. Wolters, A. J. Feijt, and C. Simmer (2009), On the sensitivity of satellite-derived cloud properties to sensor resolution and broken clouds, *AIP Conf. Proc.*, *1100*, 376–379.

Hansen, J. E., and L. D. Travis (1974), Light scattering in planetary atmospheres, *Space Sci. Rev.*, *16*, 527–610.

Hansen, J. E., M. Sato, and R. Ruedy (1997), Radiative forcing and climate response, *J. Geophys. Res.*, *102*, 6831–6864.

Hess, M., R. B. A. Koelemeijer, and P. Stammes (1998), Scattering matrices of imperfect hexagonal ice crystals, *J. Quant. Spectrosc. Radiat. Transfer*, *60*(3), 301–308.

Illingworth, A. J., et al. (2007), Continuous evaluation of cloud profiles in seven operational models using ground-based observations, *Bull. Am. Meteorol. Soc.*, *88*, 883–898.

Iwabuchi, H., and T. Hayasaka (2002), Effects of cloud horizontal inhomogeneity on the optical thickness retrieved from moderate-resolution satellite data, *J. Atmos. Sci.*, *59*, 2227–2242.

Key, J. R., and J. M. Intrieri (2000), Cloud particle phase determination with the AVHRR, *J. Atmos. Sci.*, *39*, 1797–1804.

Knap, W. H., P. Stammes, and R. B. A. Koelemeijer (2002), Cloud thermodynamic phase determination from near-infrared spectra of reflected sunlight, *J. Atmos. Sci.*, *59*, 83–96.

Lenderink, G., B. J. J. M. van den Hurk, E. van Meijgaard, A. P. van Ulden, and J. Cuijpers (2003), Simulation of present-day climate in RACMO2: First results and model developments, *Tech. Rep. KNMI 252*, R. Neth. Meteorol. Inst., De Bilt, Netherlands.

Loeb, N. G., and J. A. Coakley (1998), Inference of marine stratus cloud optical depths from satellite measurements: Does 1D theory apply?, *J. Clim.*, *11*, 215–233.

Marshak, A., S. Platnick, T. Várnai, G. Wen, and R. F. Cahalan (2006), Impact of three-dimensional radiative effects on satellite retrievals of cloud droplet sizes, *J. Geophys. Res.*, *111*, D09207, doi:10.1029/2005JD006686.

Minnis, P., D. P. Garber, D. F. Young, R. F. Arduini, and Y. Takano (1998), Parameterizations of reflectance and effective emittance for satellite remote sensing of cloud properties, *J. Atmos. Sci.*, *55*, 3313–3339.

Nakajima, T., and M. D. King (1990), Determination of the optical thickness and effective particle radius of clouds from reflected solar radiation measurements. Part 1: Theory, *J. Atmos. Sci.*, *47*, 1878–1893.

Naud, C. M., A. D. Del Genio, and M. Bauer (2006), Observational constraints on the cloud thermodynamic phase in midlatitude storms, *J. Clim.*, *19*, 5273–5288.

Oreopoulos, L., and R. Davies (1998), Plane parallel albedo biases from satellite observations. Part I: Dependence on resolution and other factors, *J. Clim.*, *11*, 919–932.

Oreopoulos, L., S. E. Platnick, G. Hong, P. Yang, and R. F. Cahalan (2009), The shortwave radiative forcing bias of liquid and ice clouds from MODIS observations, *Atmos. Chem. Phys.*, *9*, 5865–5875, doi:10.5194/acp-9-5865-2009.

Pilewskie, P., and S. Twomey (1987), Discrimination of ice from water clouds by optical remote sensing, *Atmos. Res.*, *21*, 113–122.

Platnick, S., J. Y. Li, M. D. King, H. Gerber, and P. V. Hobbs (2001), A solar reflectance method for retrieving the optical thickness and droplet size of liquid water clouds over snow and ice surfaces, *J. Geophys. Res.*, *106*, 15,185–15,199, doi:10.1029/2000JD900441.

Platnick, S. E., M. D. King, S. A. Ackerman, W. P. Menzel, B. A. Baum, J. C. Riédi, and R. A. Frey (2003), The MODIS cloud products: Algorithms and examples from Terra, *IEEE Trans. Geosci. Remote Sens.*, *41*, 459–473.

Roebeling, R. A., and E. van Meijgaard (2009), Evaluation of the daylight cycle of model-predicted cloud amount and condensed water path over Europe with observations from MSG SEVIRI, *J. Clim.*, *22*, 1749–1766, doi:10.1175/2008JCLI2391.1.

Roebeling, R. A., A. J. Feijt, and P. Stammes (2006), Cloud property retrievals for climate monitoring: Implications of differences between Spinning Enhanced Visible and Infrared Imager (SEVIRI) on METEOSAT-8 and Advanced Very High Resolution Radiometer (AVHRR) on NOAA-17, *J. Geophys. Res.*, *111*, D20210, doi:10.1029/2005JD006990.

Roebeling, R. A., H. M. Deneke, and A. J. Feijt (2008), Validation of cloud liquid water path retrievals from SEVIRI using one year of CloudNET observations, *J. Appl. Meteorol. Climatol.*, *47*, 206–222, doi:10.1175/2007JAMC1661.1.

Rosenfeld, D., E. Cattani, S. Melani, and V. Levizzani (2004), Considerations on daylight operation of 1.6-versus 3.7-μm channel on NOAA and METOP satellites, *Bull. Am. Meteorol. Soc.*, *85*, 873–881.

Schulz, J., et al. (2009), Operational climate monitoring from space: The EUMETSAT Satellite Application Facility on Climate Monitoring (CM-SAF), *Atmos. Chem. Phys.*, *9*, 1687–1709.

Stammes, P. (2001), Spectral radiance modelling in the UV-Visible range, in *IRS 2000: Current Problems in Atmospheric Radiation*, edited by W. L. Smith and Y. M. Timofeyev, pp. 385–388, A. Deepak, Hampton, Va.

Stephens, G. L., and C. D. Kummerow (2007), The remote sensing of clouds and precipitation from space: A review, *J. Atmos. Sci.*, *64*, 3742–3765.

Strabala, K. I., S. A. Ackerman, and W. P. Menzel (1994), Cloud properties inferred from 8–12 μm data, *J. Appl. Meteorol.*, *33*, 212–229.

Szczodrak, M., P. H. Austin, and P. B. Krummel (2001), Variability of optical depth and effective radius in marine stratocumulus clouds, *J. Atmos. Sci.*, *58*, 2912–2926.

Turner, D. D., S. A. Ackerman, B. A. Baum, P. E. Rivercombe, and P. Yang (2003), Cloud phase determination using ground-based AERI observations at SHEBA, *J. Appl. Meteorol.*, *42*, 701–715.

Weidle, F., and H. Wernli (2008), Comparison of ERA40 cloud top phase with POLDER-1 observations, *J. Geophys. Res.*, *113*, D05209, doi:10.1029/2007JD009234.

Wolters, E. L. A., R. A. Roebeling, and A. J. Feijt (2008), Evaluation of cloud phase retrieval methods for SEVIRI onboard Meteosat-8 using ground-based lidar and cloud radar data, *J. Appl. Meteorol. Climatol.*, *47*, 1723–1738, doi:10.1175/2007JAMC1591.1.

Zinner, T., and B. Mayer (2006), Remote sensing of stratocumulus clouds: Uncertainties and biases due to inhomogeneity, *J. Geophys. Res.*, *111*, D14209, doi:10.1029/2005JD006955.

H. M. Deneke, University of Leipzig, D-04109 Leipzig, Germany.

J. F. Meirink, B. J. J. M. van den Hurk, and E. L. A. Wolters, Climate Research and Seismology Department, Royal Netherlands Meteorological Institute, PO Box 201, NL-3730 AE De Bilt, Netherlands. (wolterse@knmi.nl)

R. A. Roebeling, Research and Development Division, Weather Services, Royal Netherlands Meteorological Institute, NL-3730 AE De Bilt, Netherlands.